photonics

MDPI

Article

A Deep Echo State Network-Based Novel Signal Processing Approach for Underwater Wireless Optical Communication System with PAM and OFDM Signals

Kexin Wang, Yihong Gao, Mauro Dragone, Yvan Petillot and Xu Wang *

School of Engineering and Physical Sciences, Heriot-Watt University, Edinburgh EH14 4AS, UK
* Correspondence: x.wang@hw.ac.uk; Tel.: +44-131-451-3775

Abstract: Underwater wireless optical communication (UWOC) plays key role in the underwater wireless sensor networks (UWSNs), which have been widely employed for both scientific and commercial applications. UWOC offers high transmission data rates, high security, and low latency communication between nodes in UWSNs. However, significant absorption and scattering loss in underwater channels, due to ocean water conditions, can introduce highly non-linear distortion in the received signals, which can severely deteriorate communication quality. Consequently, addressing the challenge of processing UWOC signals with low optical signal-to-noise ratios (OSNRs) is critical for UWOC systems. Increasing the transmitting optical power and investigating more advanced signal processing technologies to recover transmitted symbols are two primary approaches to improve system tolerance in noisy UWOC signal channels. In this paper, we propose and demonstrate the application of deep echo state networks (DeepESNs) for channel equalization in high-speed UWOC systems to enhance system performance with both PAM and QPSK-OFDM modulations. Our experimental results demonstrate the effectiveness of DeepESNs in UWOC systems, achieving error-free underwater transmission over 40.5 m with data rates up to 167 Mbps. Moreover, we compare the performance of DeepESNs to conventional echo state networks and provide suggestions on the configuration of a DeepESN for UWOC signals.

Keywords: underwater wireless optical communication; signal modulation; digital signal processing; deep echo state network; machine learning

check for updates

Citation: Wang, K.; Gao, Y.; Dragone, M.; Petillot, Y.; Wang, X. A Deep Echo State Network-Based Novel Signal Processing Approach for Underwater Wireless Optical Communication System with PAM and OFDM Signals. *Photonics* **2023**, *10*, 763. https://doi.org/10.3390/photonics10070763

Received: 24 May 2023
Revised: 22 June 2023
Accepted: 27 June 2023
Published: 2 July 2023

Copyright: © 2023 by the authors. Licensee MDPI, Basel, Switzerland. This article is an open access article distributed under the terms and conditions of the Creative Commons Attribution (CC BY) license (https://creativecommons.org/licenses/by/4.0/).

1. Introduction

A modern underwater wireless sensor network (UWSN) often consists of widely distributed underwater sensors, relay buoys, autonomous underwater vehicles (AUVs), and remotely operated underwater vehicles (ROVs) to accomplish underwater sensing, monitoring, and communication tasks [1–8]. To link the distributed nodes in an UWSN, underwater optical wireless communication (UWOC), underwater acoustic communication (UWAC), and underwater radio frequency (RF) communication (URFC) are leading candidates [1] delivering essential data around each node and providing various underwater services for scientific and commercial applications, such as water quality monitoring [5], maintaining of oil platforms [9], and life study [10].

UWOC links typically utilize green or blue light as the signal carrier, featuring the highest propagation speed in water compared to UWAC and URFC [1,11]. The bandwidth of the light is in the range of hundreds of terahertz. Most UWOC systems employ a line-of-sight configuration, effectively avoiding signal diffusion scenarios common in UWAC and URFC. This configuration also significantly enhances the security of the communication system by inhibiting eavesdropping attacks. With the advantages of ultra-high bandwidth, low latency, and enhanced security, UWOC systems present considerable potential for applications in UWSNs, particularly for tasks requiring real-time data transmission. However, underwater optical channels encounter substantial interference due to severe absorption

and scattering phenomena. Scattering occurs when light deviates from its original path due to interactions with small particles or objects in the water, thereby diffusing light throughout its propagation pathway. Meanwhile, absorption converts light energy into other energy forms, such as heat, in a UWOC channel. These factors inevitably impose constraints on the achievable link length of UWOC systems [1]. While other interferences, such as chromatic and spatial dispersions, exist within UWOC channels, they are ignored in this work due to their comparably lesser impact than the power loss induced by absorption and scattering.

To alleviate this limitation, strategies to increase the optical signal-to-noise ratio (OSNR) or adapt to a noisy signal channel can be deployed. The utilization of a higher-power light source [12] or a more sensitive photon receiver [13] can improve the system's signal-to-noise ratio (SNR), thereby facilitating longer transmission distances in water. Nevertheless, the deployment of a high-power light source commonly results in a low modulation bandwidth, thereby constraining the overall transmission capacity. Additionally, highly sensitive photonic receivers, such as single-photon avalanche diodes and photomultiplier tubes, typically require exceedingly high driving voltages (ranging from ~100 V to 1000 V). Additionally, these sensitive photonic receivers are easily impacted by interference from background noise. Therefore, UWOC systems commonly require a delicate balance of the data rate and transmission distance. For example, in [14], a high-power optical source was applied and enabled a 138-m 1-Mbps UWOC transmission. The authors in [13] employed a high-sensitivity single-photon avalanche diode to achieve a 144-m 500-bps and a 117-m 2-Mbps UWOC transmission. Meanwhile, ultra-high-speed UWOC systems were demonstrated over shorter transmission distances. The authors in [15] proposed a 30-m 500-Mbps UWOC system, while the authors in [16] illustrated a 20-m 1.5-Gbps UWOC transmission, the authors in [17] utilized a laser-based white-light source to enable a 2.3-m 8.7-Gbps UWOC transmission, and a 90-m 560-Mbps UWOC system was demonstrated in [18]. Alternatively, the adoption of advanced signal processing algorithms in UWOC systems has been shown to enhance the system's adaptability to noise and attenuation in UWOC channels with low OSNR, thus enabling a high operation bandwidth and an optimal transmission rate [19–24].

In particular, channel equalization techniques to combat interference introduced by linear or non-linear distortions are key to enable the correct re-construction of the transmitted symbols at the receiver. Several different signal equalization algorithms have been applied in UWOC systems to perform adaptive channel estimation in UWOC transmission channels, including least mean squares [19], linear minimum mean squared error [20], recursive least squares (RLS) [21], etc. In general, RLS has the best performance among them for UWOC channel estimation as it can effectively improve the signal-to-noise ratio by recursively updating the coefficients [25,26].

Beside these conventional equalization algorithms, with the fast advancement of machine learning technologies in recent years, neural networks have been employed in optical communication networks [22–24,27–30] to assist the signal processing and enhance the system's ability to resist both linear and non-linear distortion. For example, in [29], an equalizer for an underwater visible light communication (UVLC) system was built by training a convolution-enhanced long short-term memory (CE-LSTM) neural network to approximate the correct mapping from delayed channel output to originally transmitted symbols. It had comparable efficiency and performances compared with a conventional Volterra-series-based equalizer and a general LSTM-based equalizer. Ref. [30] reported a multilayer perceptron (MLP) artificial neural network (ANN) classifier which was adopted as the equalizer to double the data rates in the visible light communications link. A recurrent neural network (RNN) was proposed in [23]. RNNs have been demonstrated to be superior to MLPs in learning non-linear mappings of arbitrary complexity in processing the time-series data. However, training RNNs is a non-linear nonconvex optimization problem. Stochastic gradient descent algorithms are computational demanding and prone

to fall into local minima [31]. The exploding gradient problem can also cause unstable training and prediction performance [32].

Echo state networks (ESNs) are a type of reservoir computing (RC) which was proposed as an alternative, computationally efficient method to address these problems in RNNs [33–37]. ESNs can predict and classify multivariate time series by exploiting a sparsely connected hidden layer (the "reservoir") to create a higher-dimension representation (embedding) of their input. Their computational efficiency stems from the fact that the hidden layer is fixed, and only the weights of the connections between the hidden layer and the output need to be trained. Since the error function is quadratic with respect to the weights, the training does not suffer from vanishing/exploiting gradient problems.

To further enhance the training and prediction performance of ESNs, a layered architecture, known as the deep echo state network (DeepESN), was proposed in 2017 [38]. It is uniquely suited to handle temporal data due to its structured state space organization with multi-timescale dynamics. This structure innately aligns with the compositional nature of recurrent neural modules involved in temporal data processing. DeepESNs exhibit an optimized effectiveness in layered recurrent neural networks [39,40]. The DeepESN method has been improved and applied in multiple fields to solve different problems since its proposal [39–43]. For medical diagnosis, DeepESN can be used as a new method for the diagnosis of Parkinson's Disease (PD) [44]. In [45], based on time series analysis, a serially connected multi-reservoir echo state network (MR-ESN) is developed to conduct the prediction of solar irradiance, which has the advantages of an ESN, such as high efficiency. In short-term traffic prediction, the DeepESN is used to predict the future values of the traffic parameters of interest accurately [46]. Despite the proven ability of DeepESNs' ability to address time-series data across various domains, their application in the realm of UWOC remains unexplored.

In terms of ESN performance with different network configurations, compared to an RNN, the weights of the hidden layer in the ESN are randomly initialized, and parts of the hidden units hereby could be ineffective. A larger reservoir size makes finding a good set of hidden units easier. However, the training may present a risk of overfitting if the reservoir size is too large. Ref. [47] reported a trade-off between the size of the reservoir and/or the number of training samples, due to the memory limit. Inheriting from ESNs, a DeepESN can achieve superior performance with an optimally configured reservoir, as discussed in [48–51]. DeepESNs with different reservoir configurations have been applied to several datasets, including nonlinear autoregressive moving average (NAMA), and for predictions pertaining to users' locations, orientations, and base station associations, respectively [49]. However, these studies have addressed the DeepESNs' performance with tens or hundreds of reservoir units, which may necessitate a substantial amount of computational resources for training and prediction tasks. Regrettably, UWOC systems are typically constrained in terms of computational resources, especially for practical UWOC systems which are constrained by spatial limitations and power consumption requirements.

In this paper, DeepESN is, for the first time, applied in optical communication signal processing to minimize noise and distortion effects while enhancing the system tolerance to low signal-to-noise ratio (SNR) in signals received from UWOC channels. We built a 40.5 m error-free underwater transmission link at the date rate above 100 Mbps, where the system employed both pulse-amplitude modulation (PAM) and quadrature amplitude modulation using orthogonal frequency division multiplexing (QAM-OFDM) modulations [22]. DeepESN was applied for signal processing in the system. The improvement of bit-error rate (BER) is observed with the use of DeepESN. We also applied the recursive least squares (RLS) filter [21,52] for the signal processing as the reference to compare the performances. From the experimental results, the DeepESN exhibits a superior performance to improve the system's performance in the high-data-rate signal. We also compared the DeepESN to the ESN and proposed a suggested DeepESN configuration when addressing the UWOC signal. The range of the reservoir units' number should be from one to three times the

symbol's oversampling factors. As a trade-off between the equalization performance and training efficiency, a two- or three-layer DeepESN is recommended for UWOC systems.

2. Experiment Setup

2.1. Underwater Optical Wireless Communications System

Figure 1 illustrates the block diagram of the proposed UWOC system assisted by DeepESN. 19-bit pseudorandom binary sequences (PRBSs) were generated as data source, followed by the application of (229, 255) Reed–Solomon error correction (RSEC) to enable error-free transmission. The error-free limit of the experimental system was approximately BER = 10^{-3} [53]. Using intensity modulation/direct detection (IM/DD), the intensity of the laser is directly modulated by the baseband pulse-amplitude modulation (PAM) and DC-biased optical OFDM signal [22]. PAM signal could simplify the study on the system's transmission performance with different equalization methods and the selection of DC-biased optical OFDM was a trade-off between the system's stability and communication capacity.

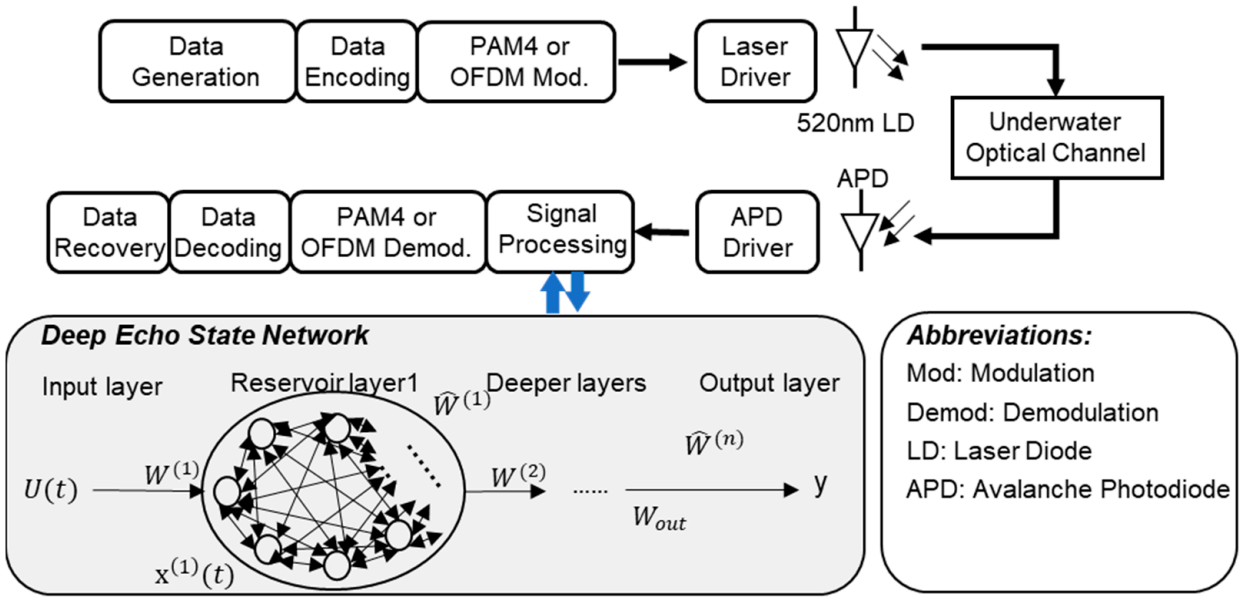

Figure 1. System configuration for deep echo state network (DeepESN)-assisted underwater wireless optical communication.

In the PAM modulation case, the encoded bits were modulated with pulse-amplitude modulation at data rates of 100, 125, and 167 Mbps, respectively. For QAM-OFDM, encoded bits were first modulated with quadrature amplitude modulation (QAM), and the time-domain OFDM signal was obtained by applying the inverse fast Fourier transformation (IFFT) to the Hermitian symmetric QAM symbols following the DC-biased optical OFDM scheme [22]. Data rates for QAM-OFDM were 100.38, 111.70, 121.21, and 130.68 Mbps. A cyclic prefix (CP) was added to the OFDM signal to avoid intersymbol interference. After signal modulation, a synchronization header was inserted into the signal frame, and pre-distortion was applied to the modulated signal to minimize the impact of the nonlinear response of the laser diode (LD). The encoded digital signal was converted to an analogy signal using a 250-Msamples/s arbitrary waveform generator (AWG). A 520-nm (green) laser was employed as the light source, and the analogy signal was internally modulated onto the optical carrier. The wireless optical signal was then transmitted through a 40.5 m underwater optical link established in a water tank.

At the receiver side, a single-pixel avalanche photodiode (APD) performed the conversion of the signal from the optical domain into the electrical domain, followed by a 250-Msamples/s oscilloscope for analogy-to-digital conversion. DeepESN was first applied

to learn and compensate for channel noise in the received digital signal prior to signal demodulation. The received PAM signal was directly demodulated. In the QAM-OFDM case, the cyclic prefix and guard band were removed from the received signal before performing QAM-OFDM demodulation. The BER was measured after RSES decoding.

In this system, an arbitrary waveform generator (RS PRO SDG6022X) was utilized to generate the analogy signal. An OSRAM PLT5 520B, yielding an average output power of approximately 16.5 dBm, served as the light source. A water tank, measuring 225 cm × 80 cm × 60 cm, generated a 40.5 m optical path by generating multiple reflections at both ends. The calculated attenuation of the UWOC channel was around 0.9 dB/m (with an attenuation coefficient of 0.207/m), approximating the conditions of clear ocean water [1]. On the receiver side, a variable attenuator (Thorlabs LCC1620A/M) was employed to attenuate the receiving power. This setup introduced a consistent power loss of 9.23 dBm at the point of least attenuation across all results. Therefore, the actual received power should be adjusted by adding this constant loss of 9.23 dBm to the observed results. The photonic receiver employed was an APD430A(/M) with a responsivity of 12 A/W. Analogy-to-digital conversion was performed using a Tektronix MDO32 oscilloscope.

2.2. Deep Echo State Network (DeepESN) Offline Training and Compensation

Figure 1 also presents the configuration of the DeepESN. To address the impact of noise introduced by UWOC channels, DeepESN offline training and compensation (DeepESN processing) were directly applied to the output signal from the oscilloscope. Digital data were first converted to the training echo states ($(\boldsymbol{X}(t) \in \mathbb{R}^{UL\times 1}$) and testing echo states ($\overline{\boldsymbol{X}}(t) \in \mathbb{R}^{UL\times 1}$) at the time instance of $t = 1, \ldots, T$ for training states or $t = T+1, \ldots, M$ for testing states. Here, U is the number of reservoir units in each reservoir layer, L is the number of reservoir layers, T is the length of the training states, and M is the total length of the states.

For the i^{th} ($i = 1, \ldots, L$) reservoir layer, the matrix product of the input weight matrix ($\boldsymbol{W}^{(1)} \in \mathbb{R}^{U\times 1}$ or $\boldsymbol{W}^{(i)} \in \mathbb{R}^{U\times U}$) and training states ($\boldsymbol{u}(t) \in \mathbb{R}^{1\times 1}$ or $\boldsymbol{x}^{(i)}(t) \in \mathbb{R}^{U\times 1}$) is fed into each reservoir layer. The echo states are calculated by [38]:

1. For the first reservoir layer (i = 1):

$$\begin{aligned} \boldsymbol{x}^{(1)}(t) &= \boldsymbol{D}\Big(\boldsymbol{u}(t), \boldsymbol{x}^{(1)}(t-1)\Big) \\ &= \Big(1-a^{(1)}\Big)\boldsymbol{x}^{(1)}(t-1) + a^{(1)}\mathbf{tanh}\Big(\boldsymbol{W}^{(1)}\boldsymbol{u}(t) + \hat{\boldsymbol{W}}^{(1)}\boldsymbol{x}^{(1)}(t-1)\Big) \end{aligned} \tag{1}$$

2. For the rest of reservoir layers (i > 1):

$$\begin{aligned} \boldsymbol{x}^{(i)}(t) &= \boldsymbol{D}\Big(\boldsymbol{x}^{(i-1)}(t), \boldsymbol{x}^{(i)}(t-1)\Big) \\ &= \Big(1-a^{(i)}\Big)\boldsymbol{x}^{(i)}(t-1) + a^{(i)}\mathbf{tanh}\Big(\boldsymbol{W}^{(i)}\boldsymbol{x}^{(i-1)}(t) + \hat{\boldsymbol{W}}^{(i)}\boldsymbol{x}^{(i)}(t-1)\Big) \end{aligned} \tag{2}$$

where $\boldsymbol{D}$ represents the echo states calculation function, **tanh** signifies the element-wise application of the hyperbolic tangent, and $\hat{\boldsymbol{W}}^{(i)} \in \mathbb{R}^{U\times U}$ denotes the recurrent weight matrix. The parameter $a^{(i)}$ refers to the leaky rate updating speed of the weight matrix in the reservoir layer and is related to the speed of reservoir dynamics in response to the input [40]. The output weight matrix $\boldsymbol{W_{out}} \in \mathbb{R}^{1\times UL}$ is obtained using the singular value decomposition (SVD) method. Equation (3) calculates the testing results utilizing the trained weight matrix [38].

$$y(t) = \boldsymbol{W_{out}}\overline{\boldsymbol{X}}(t) \tag{3}$$

In the experiment, the DeepESN has 10 reservoir units in each layer and two layers in total. This is one of the optimized setups of the DeepESN in UWOC systems, which will be discussed in the later sections.

2.3. Deep Echo State Network (DeepESN) Performance Study

DeepESN requires a large reservoir size (U) to adequately train the randomly initialized weights of its hidden layers. The network performance with different reservoir configurations has been investigated based on datasets from both simulations and practical applications [48,49]. The general conclusion is that a higher U improves the prediction performance of DeepESN, while an excessively large U may lead to substantial computational resource consumption and overfitting. Thus, reservoir configuration should be studied for different applications.

As a layered RNN architecture, DeepESN retains more information from previous inputs with a larger number of U. When the UWOC signal is fed into the DeepESN, U determines the number of previous samples used for predicting and equalizing noise or distortion in subsequent samples. In accordance with traditional equalization methods (e.g., RLS), equalizing communication signals typically requires a few prior symbols as references. For digital-to-analogy conversion, each symbol is composed of several samples ($\boldsymbol{N_{sps}}$). Consequently, value changes in adjacent samples are attributed to either noise/distortion in the UWOC channel or variations in symbols. If the reservoir size of the DeepESN is equal to an integer (m = 1, 2, 3, etc.) multiplied by $\boldsymbol{N_{sps}}$, the network is expected to achieve optimal prediction performance.

$$U = m\boldsymbol{N_{sps}} \tag{4}$$

where

$$\boldsymbol{N_{sps}} = \frac{Sampling\ Rate\ of\ ADC}{Symbol\ Rate} \tag{5}$$

Meanwhile, DeepESN will be at the risk of overfitting if m is too large.

3. Experiment Results

The time-domain characteristics of the 167 Mbps PAM signal, both with and without DeepESN processing, are depicted in Figure 2a,b. These eye diagrams illustrate the temporal properties of the PAM signal and effectively highlight the improvements brought about by DeepESN processing. Additionally, Figure 2c presents the received waveform of the 100 Mbps OFDM signal. The labels "RAW", "DESN", and "Tx" correspond to the raw signal (no signal processing), signal post DeepESN processing, and transmitted signal (reference signal), respectively.

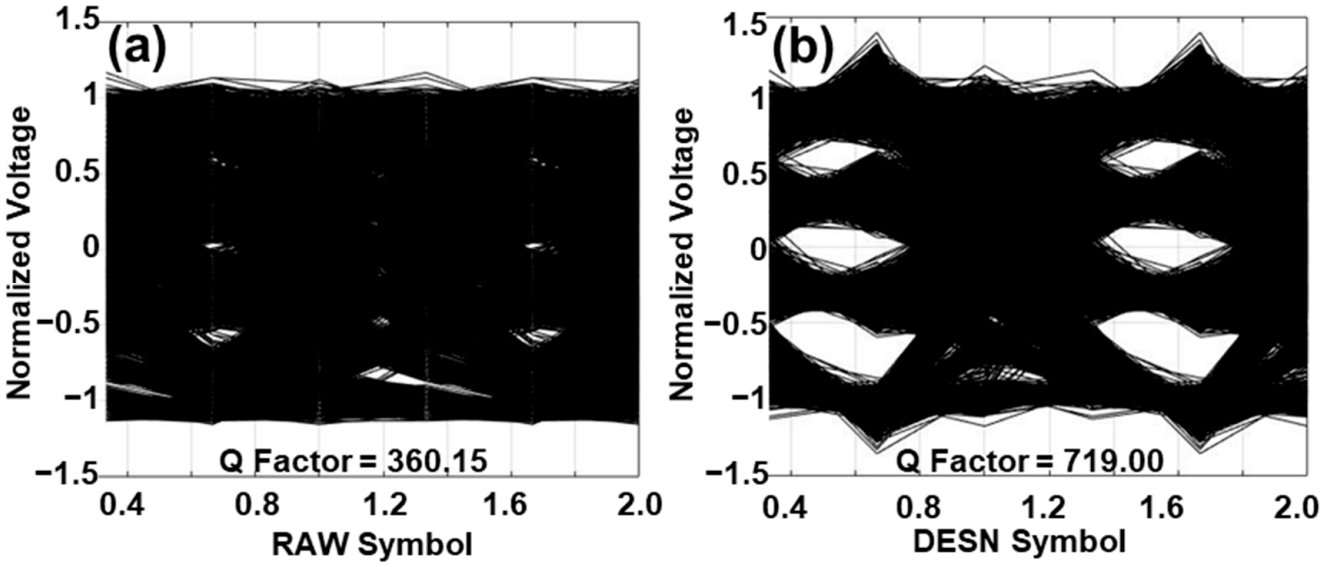

Figure 2. *Cont.*

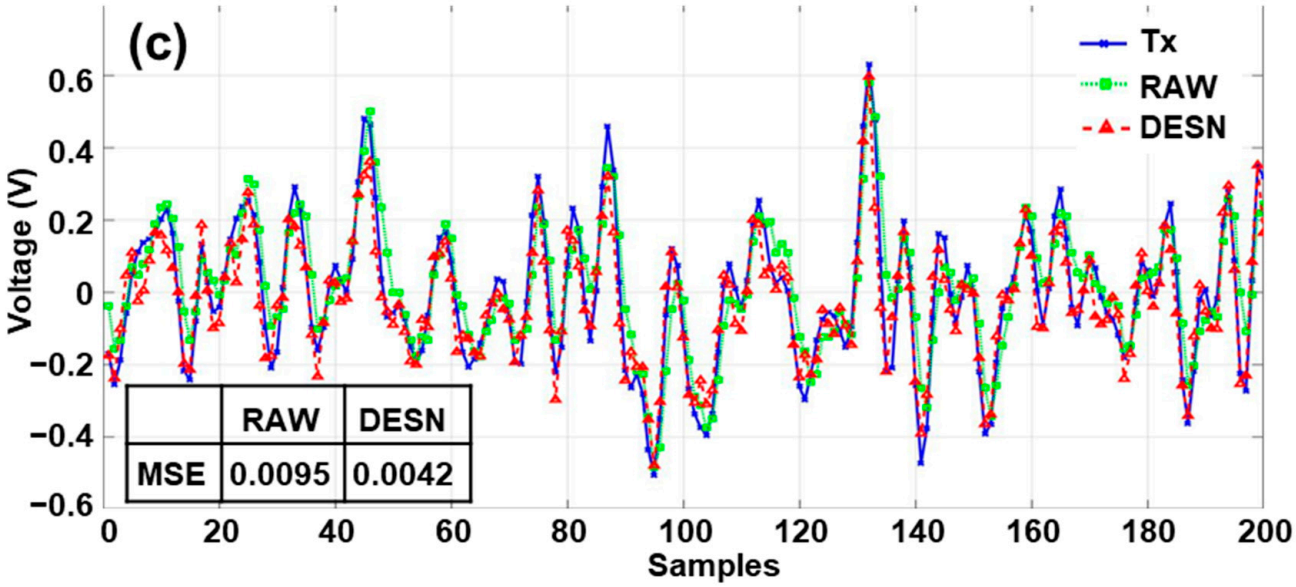

Figure 2. The eye diagrams for the 167 Mbps PAM signal (**a**) and the signal with DeepESN processing (**b**). (**c**) is the receiving waveform of the 100 Mbps OFDM signal (RAW: without equalization, DESN: with DeepESN processing, and Tx: transmitted signal). Comparing to the Tx signal, the mean square error (MSE) of RAW and DESN signals were 0.0095 and 0.0042, respectively.

3.1. PAM Modulation

In Figure 2a,b, the DESN symbols exhibit a clearer eye pattern compared to the RAW symbols. The Q factor for DESN symbols visibly surpasses that of the RAW symbols, indicating an optimal decision point of the PAM symbols. This observation implies that the BER could be improved through DeepESN processing. Figure 3a shows the BER curves for PAM4 signal processed by different equalization methods: RAW for raw signal (no signal processing), RLS for RLS equalization, and DESN for DeepESN equalization. With 250-Msamples/s signal generation/acquisition, the PAM4 signal oversampling factors are five samples per symbol (SPS) for 100 Mbps, 4 SPS for 125 Mbps, and 3 SPS for 167 Mbps. To observe the improvement of the system's transmission performance, BER curves without equalization (RAW signals) and with RLS are plotted alongside BER curves processed by DeepESN (DeepESN signals).

It can be observed that, in all cases, the BER curves reached the error-free limit as the received power gradually increased. The BER curves without equalization and with RLS (RLS signals) experienced over 3.89 dB of power penalty when the data rate increased from 100 Mbps to 167 Mbps. As the received power increased from −27.5 dBm to −20 dBm, the RLS processed signals consistently performed better than the RAW signals. The RLS processed signal's BER curves reached the error-free limit at received powers (P) of −25.2 dBm, −22.5 dBm, and −21.4 dBm for 100 Mbps, 125 Mbps, and 167 Mbps, respectively. Due to the system's nonlinear frequency response (lower response for higher frequency signals), the power penalty in RLS signals followed the trend observed in most communication systems. Figure 3a reveals a trend in BER curves: lower-data-rate signals reach its error floor more readily than those with higher data rates when they use the same equalization conditions. Furthermore, given a fixed data rate, DeepESN signals reach their error floor prior to both RAW and RLS signals. Additionally, this observation suggests that DeepESN signals exhibit better performance than RAW and RLS signals as they require less power to achieve error-free transmission.

In contrast, DeepESN signals exhibited an exceptional performance that overcomes hardware limitations and provides improved BER for higher-data-rate signals. The BER curves of DeepESN-processed signals reached 10^{-3} when $P = -21$ dBm for 100 Mbps, $P = -21.8$ dBm for 125 Mbps, and $P = -22.5$ dBm for 167 Mbps. This trend shows that

the DeepESN-processed signals performed significantly better at higher transmission rates. Higher-data-rate signals achieved better performance despite being limited by the hardware's bandwidth response.

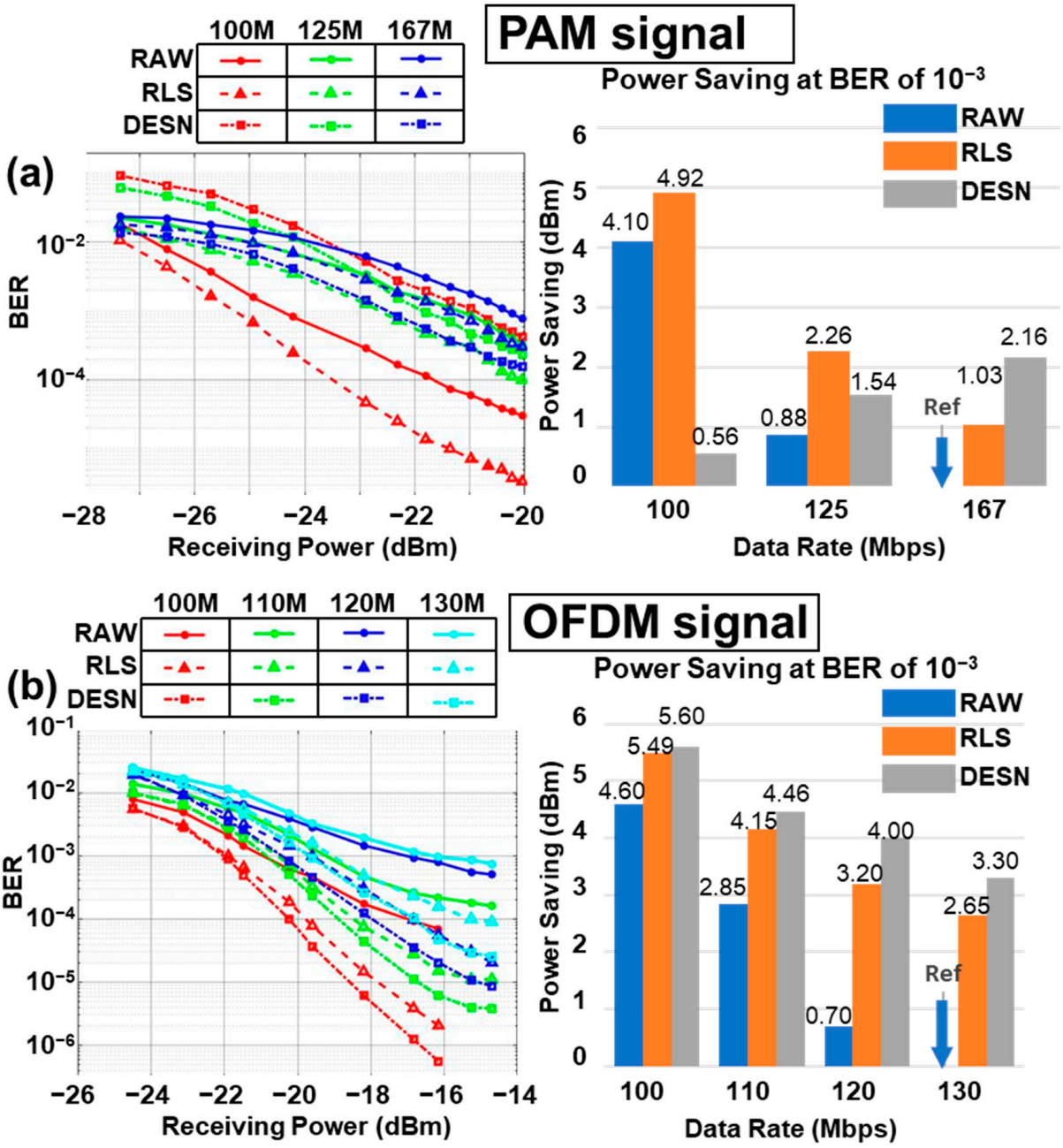

Figure 3. BER curves for PAM (**a**) and OFDM (**b**) modulations with different transmission speeds (*M for Mbps) and signal-processing methods (RAW for no equalization, RLS for recursive least squares filter, and DESN for DeepESN processing). Additionally, the power saving plot to reach the error-free limit for both PAM and OFDM is displayed.

This phenomenon is also evidenced in the power-saving plot at the right of Figure 3a. This plot illustrates the difference in received power (power saving) when the BER curves reach the error-free limit under different data rates and equalization conditions. Compared to the RAW signal at 167 Mbps, all other cases achieve a certain power saving, up to 4.92 dBm, to attain error-free transmission. For the RAW and RLS signals, their power saving decreases with the growth of the data rate. In contrast, the power saving of DeepESN

signals dramatically increases from 0.56 dBm to 2.16 dBm when the data rate rises from 100 Mbps to 167 Mbps.

3.2. QAM-OFDM Modulation

In the QAM-OFDM modulation experiment, the length of the CP was 8, and there were 3060 IFFT blocks in a data frame. The number of used subcarriers varied from 53 to 69 for different data rates, and the number of IFFT points was set at 256. Figure 3b presents the BER curves without signal processing (RAW), with RLS (RLS), and with DeepESN (DESN).

The DESN waveform in Figure 2 demonstrates a better match with the Tx waveform than the RAW waveform. Given the lower mean square error (MSE) for the DESN signals compared to the RAW signals, this suggests that DeepESN processing could also enhance the BER for the OFDM signal. From Figure 3b, it is observed that higher-data-rate signals suffer from a larger power penalty across all speeds and signal processing cases, with the power penalty exceeding 4.6 dB between 100 Mbps and 130 Mbps. Signals processed by DeepESN do not exhibit the abnormal performance observed in the PAM modulation case. The BER curves for the signal without equalization reached the error-free limit at the received power (P) of -20.2 dBm, -19.6 dBm, -18.1 dBm, and -17 dBm for 100 Mbps, 110 Mbps, 120 Mbps, and 130 Mbps, respectively. For all transmission rates, the signals processed by DeepESN and RLS outperformed the signal without any processing. DeepESN-assisted signals consistently showed better performance compared to the RLS method across all transmission rate cases at the same received power. For DeepESN-assisted signals with different transmission rates, the processed signal demonstrated better performance at the same received power when the transmission rate was lower.

The power-saving plot for the OFDM signals reveals a trend of power savings decrease for higher-data-rate signals in all equalization methods. Meanwhile, DeepESN signals consistently exhibit the highest power savings at each data rate. The power saving of DeepESN signal declines from 5.6 dBm at 100 Mbps to 3.3 dBm at 130 Mbps, referring to the RAW signal. It is worth noting that the difference of power savings between the RLS signal and DeepESN signal expands from 0.11 dBm at 100 Mbps to 0.65 dBm at 130 Mbps data rate.

3.3. The Performance Study of the Reservoir Size (U)

To verify the theoretical conclusions drawn in Section 2.3, the UWOC system performance with different DeepESN reservoir configurations is studied here. To simplify the study, the PAM signal is chosen as the objective in this section, and the receiving optical power range is from -20.24 dBm to -21.36 dBm. According to the UWOC system configuration stated in Section 2.1, $\boldsymbol{N_{sps}}$ is equal to 5, 4, and 3 for the data rates of 100, 125, and 167 Mbps, respectively. Consequently, in the study of DeepESN configuration, the range of U is from 1 to 20, including at least four PAM symbols in each reservoir.

The system performance against different receiving powers and varying numbers of reservoir units is shown in Figure 4. In line with the trend exhibited in Section 3.2, Figure 4a supports the conclusion that higher-data-rate signals receive a better improvement on transmission performance from DeepESN processing. In the floor range ($U > 8$), the BER decreases by approximately 0.2 dB and 0.4 dB between 100 and 125 Mbps cases and 125 and 167 Mbps cases, respectively.

Based on Equation (4), to achieve good training performance, the size of the reservoir must cover the samples that form one or more symbol(s). BERs reach the floor when U is no less than a certain value, which is 5 for 100 Mbps, 4 for 125 Mbps, and 3 for 167 Mbps, corresponding to $\boldsymbol{N_{sps}}$ ($m = 1$) in the received signal at each data rate. Before BERs reach the floor ($m < 1$), the considerably high value of BERs indicates the poor prediction performance of DeepESN due to insufficient training.

In the floor range, BERs experience a further decline when $2 \leq m \leq 3$, such as $U = 8$ and 12 for 125-Mbps signal ($\boldsymbol{N_{sps}} = 4$). This decline is slighter than that in the range of

$m < 1$, but DeepESN achieves better training. If U keep increasing, fluctuation is observed in all cases (where $m \geq 4$), indicating that overfitting happens in this range.

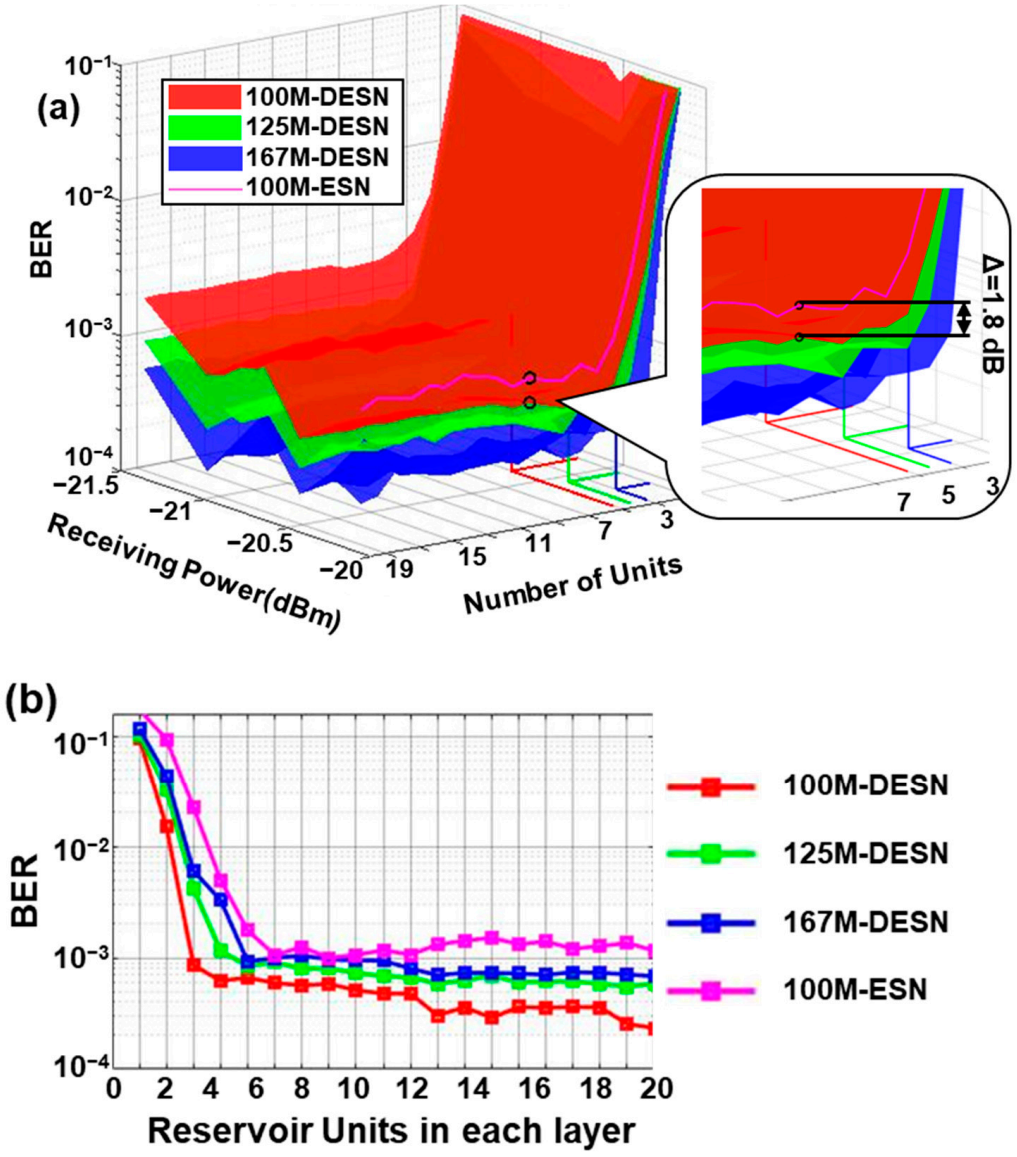

Figure 4. (**a**) The DeepESN equalization performance under different receiving powers and sizes of reservoir with different data rates. (**b**) The BER curves of DeepESN (DESN) and ESN for different data-rate signals at the receiving power of −20.05 dBm.

For the sake of comparison, a conventional ESN was also applied at the receiving power of −20.05 dBm and a data rate of 100 Mbps, as shown in Figure 4a. This follows the trend stated for DeepESN previously. The curve reaches the error floor when $U = 5$, but there is a 1.8 dB BER gap between the DeepESN and ESN results.

3.4. The Performance Study of the Number of Recurrent Layers (L) and Timing Cost

Figure 5 depicts the BER and calculation time for different numbers of recurrent layers (L) and units (U). U was fixed at 10 for the layer's curves, while the unit's curves were plotted at $L = 2$. To clearly display DeepESN performance, the 100 Mbps and −20.05 dBm signal case was selected for this part. The calculation time represents the time consumed for DeepESN training and equalization based on the Python compiler installed on a computer with an "IntelI CITM) i5-1235U" processor and 16.0 gigabytes of random-access memory (RAM).

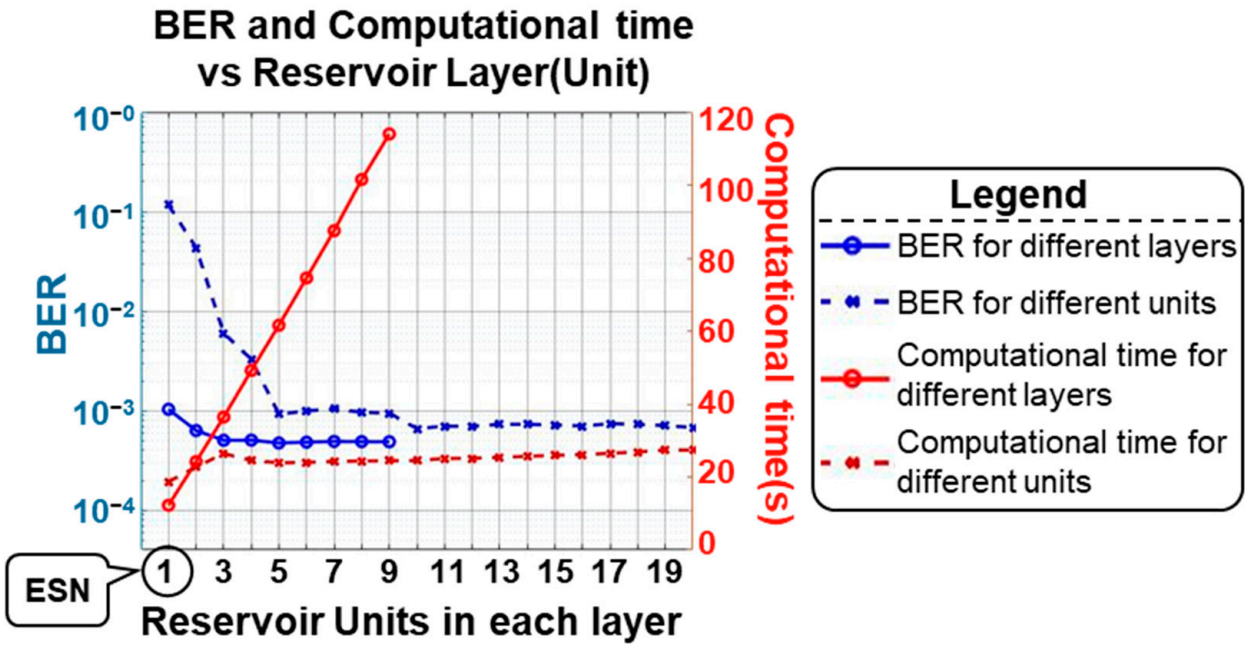

Figure 5. The BER and calculating time against different numbers of recurrent layers (L) and units (U).

As the value of L increases from 1 to 9, the BER experiences a slight decrease from 1.03×10^{-3} to 4.89×10^{-4}. However, the calculation time exhibits linear growth with a coefficient of approximately 4 s per layer. The calculation time increases rapidly when U rises to 3, but the increment afterward is relatively slow. It is worth noting that DeepESN degrades to ESN when $L = 1$. Thus, the improvement in DeepESN's equalization performance can be observed in this plot. However, deeper network configurations demand a larger amount of computational resources.

4. Discussion

4.1. DeepESN Processing for PAM and QAM-OFDM Signal

The unusual behaviour of DeepESN processing performance for PAM signals can be attributed to the fact that higher-data-rate PAM signals, compared to lower-data-rate cases, feed more symbols to DeepESN with a fixed number of training states. From an optical communications perspective, after analogy-to-digital conversion, higher-data-rate signals have a lower oversampling factor; thus, they provide more symbols for DeepESN training. For instance, for a training period of 2 milliseconds, a 100 Mbps PAM signal could provide 100,000 symbols, while a 167 Mbps signal provides approximately 167,000 symbols for DeepESN training. Additionally, in a slow time-varying channel, there is less change between $\boldsymbol{x}^{(i)}(t-1)$ and $\boldsymbol{x}^{(i)}(t)$ in higher-data-rate signals, allowing DeepESN to better learn and adapt to the slow time-varying factors in UWOC channels. Consequently, DeepESN can offer improved signal processing performance due to its inherent properties of state dynamics in layered recurrent neural architectures.

In contrast, this phenomenon was not observed for OFDM signals. This can be explained by the fact that an OFDM symbol is composed of a CP and a block of IFFT output, with each OFDM symbol occupying 264 samples. As a result, the number of reservoir units was insufficient to cover the entire OFDM symbol. Furthermore, QAM-OFDM modulation accommodates input data at different data rates by utilizing a varying number of subcarriers while maintaining the same OFDM symbol rate. Consequently, the reservoir units always cover the same portion of the OFDM symbol in different data rates. Although DeepESN processing cannot encompass an entire OFDM symbol, the enhancement in system resilience against signal deterioration with increasing data rates is evident in the power-saving plot in Figure 3b.

4.2. The Study of DeepESN Configurations on the UWOC System

To achieve optimal performance with DeepESN processing, the number of reservoir units must be large enough to cover the samples in one or two symbols to avoid insufficient training. However, overfitting occurs when the number of covered symbols is equal to or greater than four. The recommended size for each reservoir in a DeepESN ranges from $\boldsymbol{N_{sps}}$ to $\boldsymbol{3N_{sps}}$, with $\boldsymbol{2N_{sps}}$ serving as a compromise between insufficient training, overfitting, and calculation time. DeepESN offers superior signal equalization capabilities compared to conventional ESNs.

This characteristic of DeepESN also clarifies why it provides the greatest improvement in signal quality for the 167 Mbps PAM signal rather than the 100 and 125 Mbps PAM signals, as previously discussed. In the transmission experiment, the size of the reservoir was fixed at 10 units per layer. The average number of symbols that the reservoir units can cover is 3.33 for 167 Mbps, 2.5 for 125 Mbps, and 2 for 100 Mbps signals. The 167 Mbps signal hereby received the best training and compensation. This observation explains why only PAM cases experience significant signal quality improvement through DeepESN processing.

Adding more reservoir layers slightly enhances the effectiveness of DeepESN processing but it sacrifices the efficiency of the network. In a communication system, time consumption is a crucial aspect for evaluation as well, and it requires the DSP process to operate as rapidly as possible. As a result, there is a trade-off between DeepESNs' performance and efficiency. Considering the minimal decline in BER provided by configurations with more reservoir layers after $L = 3$, the suggested number of layers for DeepESN application in UWOC systems is two or three.

5. Conclusions

For the first time, the deep echo state network (DeepESN) was implemented in an optical wireless communication system to improve the system's performance for PAM and QAM-OFDM modulations. The optical signal was transmitted and received through a 40.5 m underwater channel in the experiment. The results confirm the feasibility of applying DeepESN to UWOC systems. DeepESN processing significantly improved the system's ability to reconstruct signals transmitted using both PAM and QAM-OFDM modulations, enabling power savings for the UWOC system to achieve the error-free limit. In most cases, particularly for higher-data-rate signals, DeepESN-processed signals exhibited lower BER compared to RLS-processed signals. This finding also validated DeepESN's properties in state dynamics of layered recurrent neural architectures in handling temporal data in optical communications.

This paper also investigated the training and equalization performance of DeepESN with different configurations. In line with the conclusion that the number of reservoir units determines the network's training performance from previous work, this paper emphasized the importance of selecting the appropriate number of reservoir units to avoid insufficient training and overfitting. It is recommended to set the number of reservoir units between one and three times the symbol's oversampling factors. In terms of reservoir layers, DeepESN outperforms the ESN, which only contains a single reservoir layer. Signal quality can be improved with deeper DeepESN, but increasing reservoir layers inevitably raises the calculation time. To achieve efficient and effective DSP in a UWOC system, a trade-off between equalization performance and training efficiency is essential. A two- or three-layer network is practical for general UWOC systems.

Future studies for DeepESN's application in UWOC systems could include addressing the slow time-varying distortions, such as turbulence and bubbles, which significantly impact the performance of UWOC systems. DeepESN could be a potential candidate to mitigate the effects of these distortions. In addition, other ESN configurations, such as parallel ESN, reported in Ref. [42], could also be applied for signal processing in UWOC.

Author Contributions: Conceptualization, X.W., Y.P. and M.D.; methodology, X.W. and K.W.; software, K.W. and Y.G.; validation, K.W. and Y.G.; writing and original draft preparation, K.W. and Y.G.; writing—review and editing, X.W., Y.P. and M.D.; supervision, X.W.; funding acquisition, X.W. All authors have read and agreed to the published version of the manuscript.

Funding: This research was supported by the Engineering and Physical Sciences Research Council (EP/R026173/1, EP/T001011/1).

Institutional Review Board Statement: Not applicable.

Informed Consent Statement: Not applicable.

Data Availability Statement: Data may be obtained from the authors upon request.

Acknowledgments: K.W. would like to thank Luke Erni and Issac Osahon for their support on the experiment and data processing.

Conflicts of Interest: The authors declare no conflict of interest.

References

1. Zeng, Z.; Fu, S.; Zhang, H.; Dong, Y.; Cheng, J. A Survey of Underwater Optical Wireless Communications. *IEEE Commun. Surv. Tutor.* **2017**, *19*, 204–238. [CrossRef]
2. Pompili, D.; Akyildiz, I.F. Overview of networking protocols for underwater wireless communications. *IEEE Commun. Mag.* **2009**, *47*, 97–102. [CrossRef]
3. Hosseini, E.S.; Chakraborty, M.; Roe, J.; Petillot, Y.; Dahiya, R.S. Porous Elastomer Based Wide Range Flexible Pressure Sensor for Autonomous Underwater Vehicles. *IEEE Sens. J.* **2022**, *22*, 9914–9921. [CrossRef]
4. Willners, J.S.; Carlucho, I.; Łuczyński, T.; Katagiri, S.; Lemoine, C.; Roe, J.; Stephens, D.; Xu, S.; Carreno, Y.; Pairet, È.; et al. From market-ready ROVs to low-cost AUVs. *arXiv* **2021**, arXiv:2108.05792.
5. Manjakkal, L.; Mitra, S.; Petillot, Y.R.; Shutler, J.; Scott, E.M.; Willander, M.; Dahiya, R. Connected Sensors, Innovative Sensor Deployment, and Intelligent Data Analysis for Online Water Quality Monitoring. *IEEE Internet Things J.* **2021**, *8*, 13805–13824. [CrossRef]
6. Mourya, R.; Dragone, M.; Petillot, Y. Robust Silent Localization of Underwater Acoustic Sensor Network Using Mobile Anchor(s). *Sensors* **2021**, *21*, 727. [CrossRef]
7. Mourya, R.; Saafin, W.; Dragone, M.; Petillot, Y. Ocean Monitoring Framework based on Compressive Sensing using Acoustic Sensor Networks. In Proceedings of the OCEANS 2018 MTS/IEEE Charleston, Charleston, SC, USA, 22–25 October 2018; pp. 1–10.
8. Campagnaro, F.; Signori, A.; Zorzi, M. Wireless Remote Control for Underwater Vehicles. *J. Mar. Sci. Eng.* **2020**, *8*, 736. [CrossRef]
9. Aalsalem, M.Y.; Khan, W.Z.; Gharibi, W.; Khan, M.K.; Arshad, Q. Wireless Sensor Networks in oil and gas industry: Recent advances, taxonomy, requirements, and open challenges. *J. Netw. Comput. Appl.* **2018**, *113*, 87–97. [CrossRef]
10. Salhaoui, M.; Molina-Molina, J.C.; Guerrero-González, A.; Arioua, M.; Ortiz, F.J. Autonomous Underwater Monitoring System for Detecting Life on the Seabed by Means of Computer Vision Cloud Services. *Remote Sens.* **2020**, *12*, 1981. [CrossRef]
11. Che, X.; Wells, I.; Dickers, G.; Kear, P.; Gong, X. Re-evaluation of RF electromagnetic communication in underwater sensor networks. *IEEE Commun. Mag.* **2010**, *48*, 143–151. [CrossRef]
12. Song, G.; Xu, J. Review on Long-distance Underwater Wireless Optical Communication. In Proceedings of the 2021 19th International Conference on Optical Communications and Networks (ICOCN), Qufu, China, 23–27 August 2021; pp. 1–4.
13. Chen, H.; Chen, X.; Lu, J.; Liu, X.; Shi, J.; Zheng, L.; Liu, R.; Zhou, X.; Tian, P. Toward Long-Distance Underwater Wireless Optical Communication Based on A High-Sensitivity Single Photon Avalanche Diode. *IEEE Photonics J.* **2020**, *12*, 1–10. [CrossRef]
14. Farr, N.; Ware, J.; Pontbriand, C.; Hammar, T.; Tivey, M. Optical communication system expands CORK seafloor observatory's bandwidth. In Proceedings of the OCEANS 2010 MTS/IEEE SEATTLE, Seattle, WA, USA, 20–23 September 2010; pp. 1–6.
15. Ramavath, P.N.; Acharya Udupi, S.; Krishnan, P. High-speed and reliable Underwater Wireless Optical Communication system using Multiple-Input Multiple-Output and channel coding techniques for IoUT applications. *Opt. Commun.* **2020**, *461*, 125229. [CrossRef]
16. Shen, C.; Guo, Y.; Oubei, H.M.; Ng, T.K.; Liu, G.; Park, K.-H.; Ho, K.-T.; Alouini, M.-S.; Ooi, B.S. 20-meter underwater wireless optical communication link with 1.5 Gbps data rate. *Opt. Express* **2016**, *24*, 25502–25509. [CrossRef]
17. Liu, X.; Yi, S.; Zhou, X.; Zhang, S.; Fang, Z.; Qiu, Z.-J.; Hu, L.; Cong, C.; Zheng, L.; Liu, R.; et al. Laser-based white-light source for high-speed underwater wireless optical communication and high-efficiency underwater solid-state lighting. *Opt. Express* **2018**, *26*, 19259–19274. [CrossRef]
18. Ge, W.; Du, Z.; Cai, C.; Song, G.; Qin, S.; Wang, H.; Zhang, T.; Xu, J. 90-m/560-Mbps underwater wireless optical communication utilizing subband multiple-mode full permutation CAP combined with an SNR-weighted detector and multi-channel DFE. *Opt. Express* **2023**, *31*, 13154–13168. [CrossRef] [PubMed]
19. Ghosh, A.; Barner, J.; Paparao, P. Design of least-mean-square based adaptive optical equalizers. *Opt. Commun.* **1992**, *91*, 280–292. [CrossRef]

20. Cannizzaro, R.C.; Banelli, P.; Leus, G. Adaptive Channel Estimation for OFDM Systems with Doppler spread. In Proceedings of the 2006 IEEE 7th Workshop on Signal Processing Advances in Wireless Communications, Cannes, France, 2–5 July 2006; pp. 1–5.
21. Zhang, Q. Some Implementation Aspects of Sliding Window Least Squares Algorithms. *IFAC Proc. Vol.* **2000**, *33*, 763–768. [CrossRef]
22. Jiang, R.; Sun, C.; Zhang, L.; Tang, X.; Wang, H.; Zhang, A. Deep Learning Aided Signal Detection for SPAD-Based Underwater Optical Wireless Communications. *IEEE Access* **2020**, *8*, 20363–20374. [CrossRef]
23. Kechriotis, G.; Zervas, E.; Manolakos, E.S. Using recurrent neural networks for adaptive communication channel equalization. *IEEE Trans. Neural Netw.* **1994**, *5*, 267–278. [CrossRef]
24. Mata, J.; de Miguel, I.; Durán, R.J.; Merayo, N.; Singh, S.K.; Jukan, A.; Chamania, M. Artificial intelligence (AI) methods in optical networks: A comprehensive survey. *Opt. Switch. Netw.* **2018**, *28*, 43–57. [CrossRef]
25. Yang, X.; Tong, Z.; Dai, Y.; Chen, X.; Zhang, H.; Zou, H.; Xu, J. 100 m full-duplex underwater wireless optical communication based on blue and green lasers and high sensitivity detectors. *Opt. Commun.* **2021**, *498*, 127261. [CrossRef]
26. Junejo, N.U.; Esmaiel, H.; Sun, H.; Qasem, Z.A.H.; Wang, J. Pilot-Based Adaptive Channel Estimation for Underwater Spatial Modulation Technologies. *Symmetry* **2019**, *11*, 711. [CrossRef]
27. Amirabadi, M.A. A Survey on Machine Learning for Optical Communication [Machine Learning View]. *arXiv* **2019**, arXiv:1909.05148.
28. Trichili, A.; Issaid, C.B.; Ooi, B.S.; Alouini, M.S. A CNN-Based Structured Light Communication Scheme for Internet of Underwater Things Applications. *IEEE Internet Things J.* **2020**, *7*, 10038–10047. [CrossRef]
29. Li, Z.; Hu, F.; Li, G.; Zou, P.; Wang, C.; Chi, N. Convolution-Enhanced LSTM Neural Network Post-Equalizer used in Probabilistic Shaped Underwater VLC System. In Proceedings of the 2020 IEEE International Conference on Signal Processing, Communications and Computing (ICSPCC), Macau, China, 21–23 August 2020; pp. 1–5.
30. Haigh, P.A.; Bausi, F.; Kanesan, T.; Le, S.T.; Rajbhandari, S.; Ghassemlooy, Z.; Papakonstantinou, I.; Popoola, W.; Burton, A.; Minh, H.L.; et al. A 20-Mb/s VLC Link With a Polymer LED and a Multilayer Perceptron Equalizer. *IEEE Photonics Technol. Lett.* **2014**, *26*, 1975–1978. [CrossRef]
31. Doya, K. Bifurcations in the learning of recurrent neural networks. In Proceedings of the 1992 IEEE International Symposium on Circuits and Systems, San Diego, CA, USA, 10–13 May 1992; Volume 2776, pp. 2777–2780.
32. Chatzis, S.P.; Demiris, Y. The copula echo state network. *Pattern Recognit.* **2012**, *45*, 570–577. [CrossRef]
33. Jaeger, H. Adaptive nonlinear system identification with Echo state networks. In Proceedings of the 15th International Conference on Neural Information Processing Systems, Vancouver, BC, Canada, 10–13 December 2002; pp. 609–616.
34. Tiňo, P.; Hammer, B.; Bodén, M. Markovian Bias of Neural-based Architectures With Feedback Connections. In *Perspectives of Neural-Symbolic Integration*; Hammer, B., Hitzler, P., Eds.; Springer: Berlin/Heidelberg, Germany, 2007; pp. 95–133.
35. Gallicchio, C.; Micheli, A. Architectural and Markovian factors of echo state networks. *Neural Netw.* **2011**, *24*, 440–456. [CrossRef]
36. Yildiz, I.B.; Jaeger, H.; Kiebel, S.J. Re-visiting the echo state property. *Neural Netw.* **2012**, *35*, 1–9. [CrossRef]
37. Onasami, O.; Feng, M.; Xu, H.; Haile, M.; Qian, L. Underwater Acoustic Communication Channel Modeling Using Reservoir Computing. *IEEE Access* **2022**, *10*, 56550–56563. [CrossRef]
38. Gallicchio, C.; Micheli, A.; Pedrelli, L. Design of deep echo state networks. *Neural Netw.* **2018**, *108*, 33–47. [CrossRef]
39. Gallicchio, C.; Micheli, A. Deep Echo State Network (DeepESN): A Brief Survey. *arXiv* **2017**, arXiv:1712.04323.
40. Gallicchio, C.; Micheli, A.; Pedrelli, L. Deep reservoir computing: A critical experimental analysis. *Neurocomputing* **2017**, *268*, 87–99. [CrossRef]
41. Gallicchio, C.; Micheli, A. Deep Tree Echo State Networks. In Proceedings of the 2018 International Joint Conference on Neural Networks (IJCNN), Rio de Janeiro, Brazil, 8–13 July 2018; pp. 1–8.
42. Gallicchio, C.; Micheli, A. Experimental Analysis of Deep Echo State Networks for Ambient Assisted Living. In Proceedings of the 16th International Conference of the Italian Association for Artificial Intelligence, Bari, Italy, 14–17 November 2017.
43. Gallicchio, C.; Micheli, A. Why Layering in Recurrent Neural Networks? A DeepESN Survey. In Proceedings of the 2018 International Joint Conference on Neural Networks (IJCNN), Rio de Janeiro, Brazil, 8–13 July 2018; pp. 1–8.
44. Gallicchio, C.; Micheli, A.; Pedrelli, L. Deep Echo State Networks for Diagnosis of Parkinson's Disease. *arXiv* **2018**, arXiv:1802.06708.
45. Li, Q.; Wu, Z.; Ling, R.; Feng, L.; Liu, K. Multi-reservoir echo state computing for solar irradiance prediction: A fast yet efficient deep learning approach. *Appl. Soft Comput.* **2020**, *95*, 106481. [CrossRef]
46. Ser, J.D.; Laña, I.; Manibardo, E.L.; Oregi, I.; Osaba, E.; Lobo, J.L.; Bilbao, M.N.; Vlahogianni, E.I. Deep Echo State Networks for Short-Term Traffic Forecasting: Performance Comparison and Statistical Assessment. In Proceedings of the 2020 IEEE 23rd International Conference on Intelligent Transportation Systems (ITSC), Rhodes, Greece, 20–23 September 2020; pp. 1–6.
47. Lukoševičius, M.; Jaeger, H. Reservoir computing approaches to recurrent neural network training. *Comput. Sci. Rev.* **2009**, *3*, 127–149. [CrossRef]
48. Liu, X.; Chen, M.; Yin, C.; Saad, W. Analysis of Memory Capacity for Deep Echo State Networks. In Proceedings of the 2018 17th IEEE International Conference on Machine Learning and Applications (ICMLA), Orlando, FL, USA, 17–20 December 2018; pp. 443–448.
49. Chen, M.; Semiari, O.; Saad, W.; Liu, X.; Yin, C. Federated Echo State Learning for Minimizing Breaks in Presence in Wireless Virtual Reality Networks. *IEEE Trans. Wirel. Commun.* **2020**, *19*, 177–191. [CrossRef]

50. Gallicchio, C.; Micheli, A. Echo State Property of Deep Reservoir Computing Networks. *Cogn. Comput.* **2017**, *9*, 337–350. [CrossRef]
51. Chen, M.; Saad, W.; Yin, C.; Debbah, M. Echo State Networks for Proactive Caching in Cloud-Based Radio Access Networks With Mobile Users. *IEEE Trans. Wirel. Commun.* **2017**, *16*, 3520–3535. [CrossRef]
52. Tian, T.; Wu, F.; Yang, K. Estimation of Underwater Acoustic Channel via Block-Sparse Recursive Least-Squares Algorithm. In Proceedings of the 2019 IEEE International Conference on Signal Processing, Communications and Computing (ICSPCC), Dalian, China, 20–22 September 2019; pp. 1–6.
53. Tang, X.; Kumar, R.; Sun, C.; Zhang, L.; Chen, Z.; Jiang, R.; Wang, H.; Zhang, A. Towards underwater coherent optical wireless communications using a simplified detection scheme. *Opt. Express* **2021**, *29*, 19340–19351. [CrossRef]

Disclaimer/Publisher's Note: The statements, opinions and data contained in all publications are solely those of the individual author(s) and contributor(s) and not of MDPI and/or the editor(s). MDPI and/or the editor(s) disclaim responsibility for any injury to people or property resulting from any ideas, methods, instructions or products referred to in the content.